Temperature-dependent full spectrum dielectric function of semiconductors from first principles

Zherui Han [1], Changkyun Lee,[2] Jiawei Song,[3] Haiyan Wang [3], Peter Bermel [2], and Xiulin Ruan [1,*]

[1]*School of Mechanical Engineering and the Birck Nanotechnology Center, Purdue University, West Lafayette, Indiana 47907-2088, USA*
[2]*School of Electrical and Computer Engineering and the Birck Nanotechnology Center, Purdue University,*
West Lafayette, Indiana 47907-2088, USA
[3]*School of Materials Engineering, Purdue University, West Lafayette, Indiana 47907-2088, USA*

From the ultraviolet to the mid-infrared region, light-matter interaction mechanisms in semiconductors progressively shift from electronic transitions to phononic resonances and are affected by temperature. Here, we present a unified temperature-dependent treatment of both electrons and phonons entirely from first principles, enabling the prediction of a full-spectrum dielectric function with CeO_2 as the prototype material. At elevated temperatures, *ab initio* molecular dynamics is employed to find thermal perturbations to electronic structures and construct effective force constants describing potential energy surface. Four-phonon scattering and phonon renormalization are included in an integrated manner in this approach. Our first-principles-calculated refractive index of CeO_2 agrees well with measured data from literature and our own temperature-dependent ellipsometer experiment.

Study of temperature-dependent light-matter interactions is generally missing from the theoretical side, as most optical applications only concern room temperature and constant optical parameters are always assumed. Following a surge in recent research into high-temperature or transient nanophotonics, plasmonics, and near-field radiation, an understanding of temperature evolution of optical properties is now generally needed [1–3]. Beside the interest of uncovering the physical mechanism behind this temperature evolution, accurate prediction also has technological importance: In thermophotovoltaics (TPV) [4], heat-assisted magnetic recording technique (HAMR) [5], and thermal barrier coatings (TBC) [6], high-temperature optical properties are crucial for their realizations and performances.

Optical properties of metals at elevated temperatures have been studied both experimentally and theoretically [2,7–9]. Challenges are greater for semiconductor modeling since various elementary excitations or quasiparticles and their interplay need to be captured as a function of temperature [10,11]. An even greater challenge is to have full spectrum predictions with temperature dependence as various technologies do concern both a wide range of photon wavelengths and working temperatures, and the mechanism shifts from *electron mediated* to *phonon mediated* depending on photon wavelength. Generally, the optical properties depend on the electromagnetic field coupling with various model oscillators in solids. In semiconductors these oscillators can be excitons, optical phonons, and potentially plasmons, with different coupling strength between the oscillator and electromagnetic field, and different oscillating frequency and damping strength of the resonance [10]. In the ultraviolet, visible, and near-infrared (UV-Vis-NIR) range, the primary interaction is between the electrons and photon (e.g., interband electronic excitations), while in the mid-infrared (MIR) region where incident photon energy is much lower, IR-active phonon resonances play the major role. Earlier studies [12–15] limited to wavelengths smaller than 1.2 μm have elucidated the dynamical effect in *electron-mediated* optical responses. Recent work [11] in the weak-coupling regime of the two-dimensional (2D) systems finds a similar research gap in radiative linewidths, where 2D excitons are extensively studied but not phonons. The fact that a complete and rigorous first-principles approach is still generally lacking motivates us to investigate both *electron-mediated* and *phonon-mediated* optical processes as a function of temperature in general semiconductors.

This work considers the recent advances in first-principles techniques and temperature-dependent theories to enable a parallel, broadband treatment of both photon-electron and photon-phonon interactions in cerium dioxide (CeO_2), a dielectric ceramic. The intrinsic resemblance of basic oscillators in optical responses make it possible for us to conceive a general and parallel approach. In particular, we capture the thermal perturbations by performing *ab initio* molecular dynamics (AIMD) simulations to represent the statistical variations of physical quantities at a certain temperature. For the electron renormalization, roughly three types of first-principles approaches are available [16]. The AIMD approach treats the eigenenergies as the time average of simulation steps. The Allen-Heine-Cardona (AHC) formalism is based on perturbation theory. The frozen phonon scheme directly computes each normal mode contribution to electron energies. Past studies have pointed out the equivalency of MD at constant volume, frozen phonon scheme, and AHC formalism when the non-rigid-ion terms are included [16], but MD suffers from large computational cost and was only practical

*ruan@purdue.edu

for small supercell-size structures [13,16–18]. In this study, we overcome this drawback and use a large enough system with around 200 atoms for AIMD simulations. Our methodology on electron renormalization then has three improvements compared to the previous works: (i) It uses a large enough system to sample the phonon wave-vector space; (ii) it naturally includes thermal expansion by switching ensembles in AIMD simulation; (iii) it enables a unified MD approach for both electron and phonon renormalizations. We obtain temperature-dependent electronic and phononic structures by averaging the snapshots in AIMD or fitting an effective potential to get their renormalized energies, respectively. Dielectric function can further be calculated from electronic transitions [19] in UV-Vis-NIR and application of the Lorentz oscillator model [20] in the MIR region. The key physical parameters involved in this process are band structure and phonon self-energy (both real and imaginary parts), and we are able to resolve their temperature dependence concurrently. Specifically, we include phonon renormalization and four-phonon scattering [21] in the calculation of phonon energy and damping factor. In this study, we choose crystal CeO_2 as a benchmark material considering its broad technological importance, especially in high-temperature applications such as oxide fuel cells and gas sensors [22,23], but the methodology above can be extended to dielectrics and semiconductors in general. We find that the imaginary part of the dielectric function increases, and refraction peak undergoes a red shift and a reduction in peak value with rising temperatures. Due to the reduction of the band gap, lower energy photons can be absorbed as the temperature increases. For wavelengths longer than 500 nm, the refractive index increases with temperature. Our own temperature-dependent ellipsometer measurements confirm the temperature trend of our calculated refractive index and validate our theoretical approach. This paper is organized as follows. After a brief discussion on computational techniques, we describe the process of obtaining the electronic band structure and phonon dispersions as a function of temperature. Then we present the computation of dielectric functions that span from the UV-Vis-NIR to MIR range as a function of temperature. Finally we compare our temperature-dependent full spectrum refractive index with our own measurements.

The dielectric function, representing the optical responses of the system, is computed by perturbation theory and the Lorentz oscillator model for the UV-Vis-NIR and MIR region, respectively. The expression for the imaginary part of dielectric tensor $\text{Im}[\epsilon(\omega)]_{\alpha\beta}$ due to electronic transitions is [19]

$$\text{Im}[\epsilon(\omega)]_{\alpha\beta} = \frac{4\pi^2\hbar^4 e^2}{\Omega\omega^2 m_e^2} \lim_{q\to 0} \sum_{c,v,\mathbf{k}} 2w_{\mathbf{k}}\delta(\epsilon_{c\mathbf{k}} - \epsilon_{v\mathbf{k}} - \omega)$$
$$\times \langle u_{c\mathbf{k}} \mid i\nabla_\alpha - \mathbf{k}_\alpha \mid u_{v\mathbf{k}}\rangle\langle u_{v\mathbf{k}} \mid i\nabla_\beta - \mathbf{k}_\beta \mid u_{c\mathbf{k}}\rangle^*,$$
(1)

where Cartesian directions are denoted by $\alpha\beta\gamma$, Ω is the unit cell volume, $w_{\mathbf{k}}$ is the weights for k-point $\mathbf{k}$, and ϵ is the electron energy with c and v denoting conduction band and valence band, respectively. The notation $u_{c\mathbf{k}}$ is the cell periodic part of the orbitals at $\mathbf{k}$ and ∇ is the momentum operator. The real part of the dielectric function $\text{Re}[\epsilon(\omega)]$ is

further calculated by the Kramers-Kronig transformation. In CeO_2, $\epsilon(\omega)$ is isotropic. The above expression requires band energies at finite temperature. Turning to the MIR region with phonon resonances, $\epsilon(\omega)$ is determined by a four-parameter Lorentz oscillator model [24,25]:

$$\epsilon(\omega) = \epsilon_\infty \prod_m \frac{\omega_{m,\text{LO}}^2 - \omega^2 + i\omega\gamma_{m,\text{LO}}}{\omega_{m,\text{TO}}^2 - \omega^2 + i\omega\gamma_{m,\text{TO}}},$$
(2)

where ϵ_∞ is the dielectric constant at a high-frequency limit that can be calculated by perturbation theory. LO and TO in the subscript denote the longitudinal and transverse optical phonons, respectively. ω_m is the resonance phonon frequency and γ_m is the phonon damping factor corresponding to the m-th IR-active phonon modes, and $\epsilon(\omega)$ is the summation of all IR-active phonon resonances. This damping factor γ is related to the phonon-phonon scattering rate τ^{-1} by $\gamma = (\tau^{-1}/2\pi)$. Such a model requires temperature-dependent IR-active phonon energies and their scattering rates. To summarize, to compute dielectric function for the full spectrum, one needs temperature-dependent energy carrier energies and their coupling with photons. In this study, we compute these quantities from first principles.

All first-principles calculations are performed in the framework of density functional theory (DFT) or density functional perturbation theory (DFPT) as implemented in Vienna *Ab initio* Simulation Package (VASP) [26], including AIMD simulations and single-point calculation using the finite difference method to obtain anharmonic interatomic force constants. Phononic structure and the phonon damping factor are calculated utilizing the PHONOPY [27] and FOURPHONON packages [28,29]. Further computational details are presented in Supplemental Material [30]. A known drawback of standard DFT for ceria-based materials is the poor description of the Ce $4f$ state, and this is normally remedied by adding a Hubbard U term [31]. We follow the suggestion in Ref. [32] and use the local density approximation with the Hubbard parameter (LDA+U) approach by setting $U_{\text{eff}} = 10\,\text{eV}$ in this study to correct our band structure. The simulated band gap (2.97 eV) is within the reported experimental range [33,34]. We note that a more advanced approach to study the quasi-particle properties is the *ab initio* GW method [35], where the electron self-energy is linearly expanded in the screened Coulomb interaction (W). In addition, GW plus the Bethe-Salpeter equation (GW+BSE) method [36,37] is proven to be successful to evaluate band gaps and optical properties in various material systems [38] with recent applications to lanthanide oxides including ceria [39,40]. More recently, the many-electron correlation with Møller-Plesset perturbation theory also shows a good description of the Ce $4f$ subshell [41].

A central issue is how we incorporate temperature into dispersion relations of two different energy carriers and obtain renormalized energy. Temperature renormalization of the electronic band structure originates from thermal expansion and electron-phonon interactions (EPI) [42]. One theoretical approach [43] to renormalize the band structure is to treat these two effects analytically by computing thermally expanded lattice and evoking AHC formalism [42,44], respectively. This analytical approach conveys a clear physical
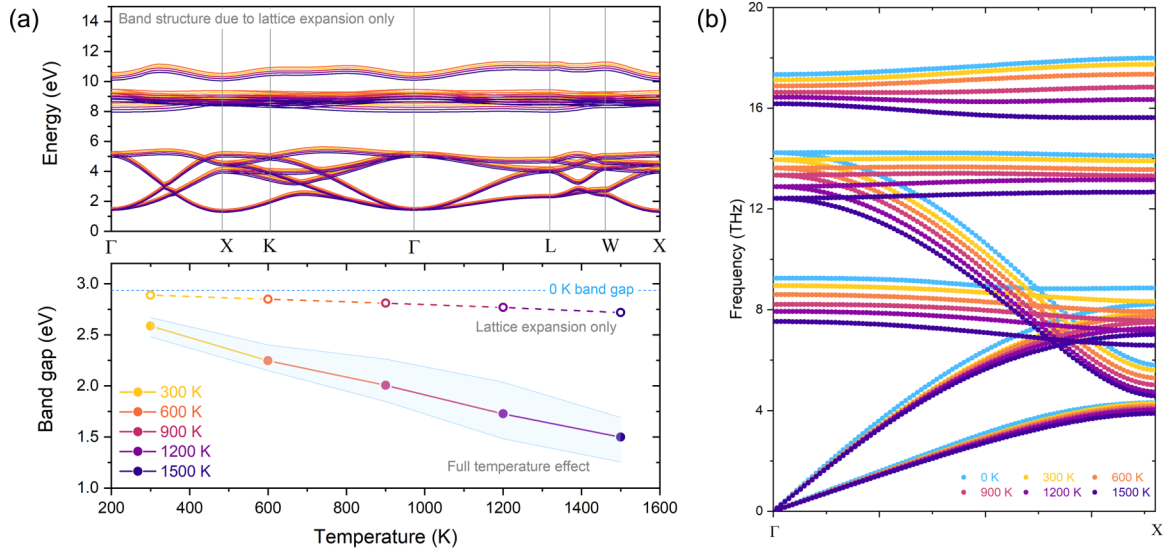
FIG. 1. Temperature-dependent band structure and phonon dispersions. (a) Band structure with lattice expansion only (top), and the band gap as a function of temperature (bottom) when only lattice expansion is considered (dashed line) or dynamical effect is included (solid line). (Top) Band structure at each T is obtained by non-self-consistent DFT calculations at relaxed unit cell structure that comes from AIMD simulations under NPT ensemble. (Bottom) Data points of full effect are the averaged band gap values calculated from 10 snapshots in AIMD simulations and the shaded area is the span of those 10 gap energies at each T. DFT band gap at 0 K is shown in blue dotted vertical line as a reference. (b) Phonon dispersions at finite T. All phonon energies are reduced with rising temperatures. Longitudinal and transverse optical phonon splitting is treated by considering long-range interactions using Born effective charge calculated by DFPT [27].

picture but is limited to harmonic effects [45]. It is suggested that when the non-rigid-ion terms are included, AHC theory should be equivalent with MD at constant volume [16]. Future study can be devoted to compare our AIMD simulations to explicit EPI calculations. To have a consistent methodology for both electron and phonon renormalization, we need to capture anharmonic effect. AIMD simulation naturally considers thermal disorder [46] and in the following discussion we would detail our parallel approach to renormalize both electron and phonon self-energies using AIMD. We start by bringing the system to a certain temperature T (up to 1500 K) using AIMD under a NPT ensemble with zero external pressure. The simulation is performed on a supercell structure consisting of 192 atoms constructed by $4 \times 4 \times 4$ primitive cells. After reaching equilibrium, we find the relaxed structure at T. For CeO_2, we simulate the linear thermal expansion coefficient to be $\alpha = 1.05 \times 10^{-5}$ K^{-1} while the experimental reported value is around 1.16×10^{-5} K^{-1} [47]. On top of this relaxed structure at every T, we perform AIMD under a NVT ensemble to sample the thermal perturbations. For electronic structure, we randomly choose 10 snapshots of NVT simulations and we calculate their band energies individually. This part of the treatment is similar to Refs. [46,48] as we find the T-dependent band gap by averaging snapshots, but the supercell system in our calculation is much larger. Figure 1(a) shows our calculated band structure, band gap due to thermal expansion only and the band gap due to temperature disorder altogether. The averaged band gap decreases with temperature, which is a result of both thermal expansion and EPI in semiconductors [48,49]. We observe from the band structure with relaxed atomic structure at certain T [see top panel and dashed line in the bottom panel of Fig. 1(a)] that the reduction due to lattice expansion is quite small,

suggesting that in CeO_2 the dynamical effect from EPI is more pronounced than the lattice expansion. Also, the contribution from EPI is stronger at higher temperatures. Our calculated band gap evolution has a linear slope of -9.53×10^{-4} eV/K, in agreement with a recent measurement up to 800 K [50] which is reported to be -9.76×10^{-4} eV/K. This agreement of temperature evolution supports our AIMD approach to capture the dynamical effect of electronic structure.

Now we turn to phonon dispersions, which are relevant to resonances in the MIR range. For phonons, we apply a temperature-dependent effective potential method (TDEP) that uses the force-displacement data set $\{\mathbf{F}_t^{MD}, \mathbf{U}_t^{MD}\}$ in N_t time steps in NVT simulations to construct effective harmonic force constants Φ_2^* (HFCs) [51] that can best describe the potential landscape at certain T. The method aims to minimize the difference between the model harmonic system and MD [51]:

$$\min_{\Phi_2^*} \Delta \mathbf{F} = \frac{1}{N_t} \sum_{t=1}^{N_t} \left| \mathbf{F}_t^{MD} - \mathbf{F}_t^{H} \right|^2, \qquad (3)$$

where $\mathbf{F}_t^{H}$ is the force calculated from the effective harmonic system $\mathbf{F}_t^{H} = \Phi_2^* \mathbf{U}_t^{MD}$ in the t-th time step. This effective HFC then intrinsically includes the effect of anharmonic phonon-phonon interactions on the phonon frequency [52] and renormalizes the phonon energies. Note that the structure at certain T is the relaxed structure. Figure 1(b) presents our calculated phonon dispersions at a function of temperature using the effective HFCs. High temperature softens the phonon energies, especially the optical phonon branches. Since IR optical responses reply on IR-active phonon modes, this softening is expected to shift the resonance peak observed in the optical spectrum.

With the temperature-dependent energy carrier spectrum, we then proceed to calculate dielectric function in the UV-Vis-NIR and MIR ranges.

(1) Dielectric function due to electronic transitions in the UV-Vis-NIR range is the average of dielectric functions of all the collected snapshots [13]. Each snapshot is a perturbed supercell structure in AIMD simulation. We note that calculating dielectric function of a large supercell (192 atoms in our case) is nontrivial as the enlarged supercell structure has band folding in the reduced Brillouin zone. To address this issue and to reach convergence in DFT calculations, we include 2560 empty bands to allow sufficient electronic transitions in our first-principles calculations.

(2) For the dielectric function due to phonon resonances, we consider the recent theoretical advancements that single out the importance of phonon renormalization and higher-order anharmonicity in the prediction of optical phonon scatterings [21,53], where optical phonon frequencies are renormalized [see Fig. 1(b)] and the phonon-phonon scattering has two-channel contributions: $\tau^{-1} = \tau_{3ph}^{-1} + \tau_{4ph}^{-1}$, i.e., three- ($\tau_{3ph}^{-1}$) and four-phonon ($\tau_{4ph}^{-1}$) scattering. The renormalized phonon energy and the effective third- and fourth-order force constants [54,55] are all obtained through AIMD simulations in this work, so as to be consistent with our treatment of the electronic band structure.

Our calculated dielectric function $\epsilon(\omega)$ for the whole spectrum is presented in Fig. 2. The comparison with room-temperature measurement [56] is presented in the Supplemental Material [30]. In this plot, we compare the real and imaginary parts of the complex dielectric function at 0 and 900 K. In the UV-Vis-NIR range shown in Fig. 2(a), the first absorption peak in Im[$\epsilon(\omega)$] is correlated with the band gap reduction we present in Fig. 1(a): At higher temperature, lower photon energy is required to have interband transitions. This indicates that the material becomes more metallic. Another signature of temperature effect is the broadened peaks in both Re[$\epsilon(\omega)$] and Im[$\epsilon(\omega)$], which can be attributed to the structure disorder induced by stronger lattice vibrations. Note that this is captured in our AIMD simulations and averaging procedure. In contrast, the $\epsilon(\omega)$ with only lattice expansion considered (dashed lines) at 900 K shows shifts in peak energies but no broadening. This behavior reconciles with our observation from Fig. 1(a) that lattice thermal expansion has a minor effect on renormalized band structure. Turning to the MIR range shown in Fig. 2(b), we find that Re[$\epsilon(\omega)$] becomes more negative with temperature while Im[$\epsilon(\omega)$] decreases. This suggests that at higher temperature CeO_2 has larger dielectric loss with a larger damping factor. Also, we observe that Im[$\epsilon(\omega)$] has larger temperature dependence while the difference in Re[$\epsilon(\omega)$] is marginal. At 900 K, using a conventional approach that includes only three-phonon (3ph) scattering and no phonon renormalization effect (dashed cyan lines), Re[$\epsilon(\omega)$] is almost unaffected but Im[$\epsilon(\omega)$] is larger compared to the full effect. Further inclusion of four-phonon (4ph) scattering gives similar results (dash-dot orange line). Phonon renormalization then brings both 3ph and 4ph scattering back to a lower level (solid blue line). This is understood as phonon renormalization weakens the phonon scattering, and in the case of CeO_2 this effect is stronger than the sole
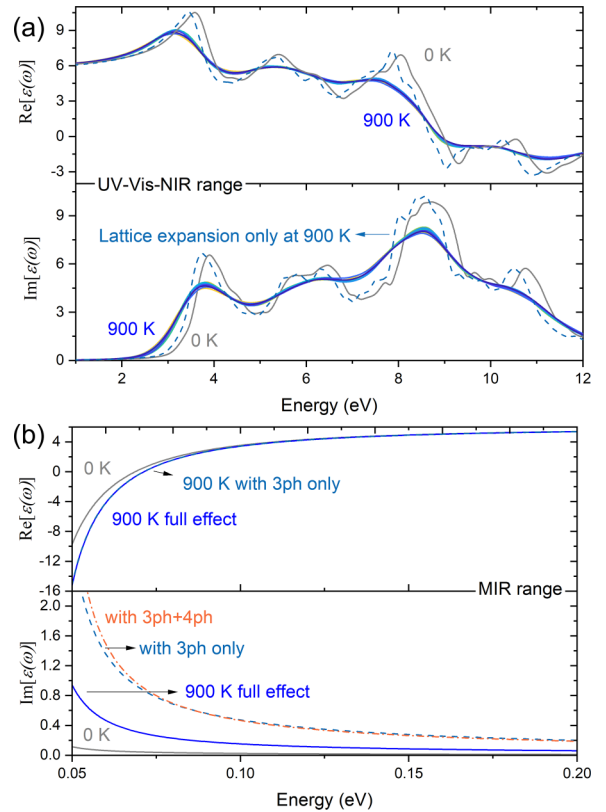

FIG. 2. Dielectric function $\epsilon(\omega)$ at 0 K (gray lines) and 900 K (blue lines). (a) $\epsilon(\omega)$ from electronic transition in the UV-Vis-NIR range. Each colored solid line represents the dielectric function for one snapshot structure in AIMD simulations. Dashed lines are $\epsilon(\omega)$ calculated on the relaxed structure at 900 K. (b) $\epsilon(\omega)$ from phonon resonances in the MIR range. Damping factor for 0 K is approximated by scattering rates at 5 K. Dashed cyan lines represent $\epsilon(\omega)$ with only 3ph scattering included. Dash-dot orange line represents $\epsilon(\omega)$ with 3ph+4ph scattering included. Solid lines represent $\epsilon(\omega)$ with both 3ph and 4ph scattering and phonon renormalization. In the top panel of (b), the dashed line nearly overlaps with the solid line.

inclusion of 4ph scattering to correct the conventional 3ph approach.

With the full spectrum temperature-dependent dielectric function $\epsilon(\omega)$, we can easily relate to the refractive index, a more relevant optical quantity in applied fields, by using the relation $\epsilon = (n + i\kappa)^2$, where n and κ are the real and imaginary parts of the complex refractive index, respectively. To validate our first-principles computed results, we also measure n and κ at different temperatures using ellipsometry, where the measured amplitude ratio ϕ and phase difference Δ between the p and s polarizations are fitted into a Cauchy dispersion model to obtain the refractive index as a function of wavelength. The experiments are performed on a CeO_2 thin film sample that is deposited on a STO (001) substrate kept at 600 °C by using pulsed laser deposition (PLD) with a KrF excimer laser. Details of this optical measurement and sample preparation are presented in Supplemental Material [30]. Our calculated results and experimental measurements are shown in Fig. 3. Two other literature measurements are also presented for comparison [57,58]. For wavelength longer than
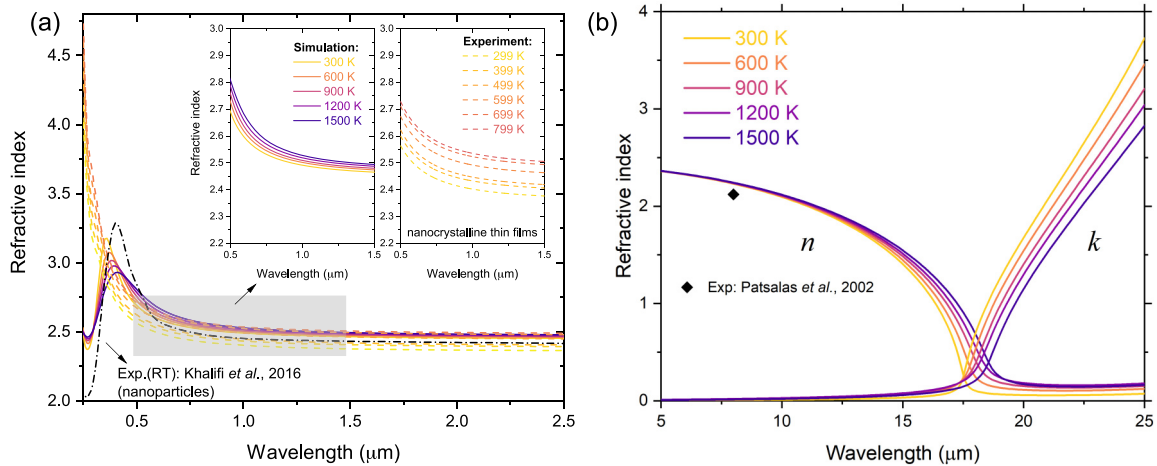
FIG. 3. Temperature-dependent full spectrum refractive index. (a) Simulated refractive index (solid colored lines) with our ellipsometry measurement (dashed colored lines) up to 2.5 μm and from 300 to 800 K, and an earlier measurement (black dash-dotted line) on CeO$_2$ nanoparticles [57] at room temperature. Imaginary part κ is nearly zero in this range. (b) Simulated refractive index (solid colored lines) with an earlier measurement [58] (black diamond) in the MIR range.

0.5 μm, refractive index n increases with rising temperatures and this trend is consistent up to 800 K in experiment. This implies that the material is more reflective at higher temperatures. We note that the observed variation of n is greater than what is predicted by first-principles calculations. Possible reasons include grain boundary or defect scattering induced by finite grain size or potential oxygen vacancies in our CeO$_2$ nanocrystalline thin films. The first-principles calculation has assumed a perfect single crystal structure. To further demonstrate this argument, we perform another set of temperature-dependent measurements on a thinner sample, as presented in Sec. 3 of Supplemental Material [30]. Another signature is the redshift of the first absorption peak around 0.4 μm or 3 eV, which is due to band gap reduction at higher temperatures. This change is consistent across the energy spectrum in Fig. 1(a), dielectric response in Fig. 2(a), and finally the optical response presented in Fig. 3(a). Turning to the MIR range in Fig. 3(b), real part n has a weak temperature dependence while the extinction coefficient κ decreases with temperatures.

To summarize, we have established a first-principles framework for calculating temperature-dependent optical responses in the full spectrum of semiconductors. This is enabled by a parallel treatment of electrons and phonons at finite temperature using AIMD. On top of the thermally relaxed structure extracting from the NPT ensemble, we capture the thermal perturbations from further NVT ensemble configurations and obtain renormalized electron and phonon energies. The dielectric function for the whole spectrum is then computed by electronic transitions in UV-Vis-NIR and the Lorentz oscillator model in the MIR range. The computed refractive index as a function of temperature is in good agreement with our own ellipsometric measurement on CeO$_2$ thin film. The first-principles methodology demonstrated in this study can have important implications in both optics and the thermal radiation community.

[1] C. R. Otey, W. T. Lau, and S. Fan, Thermal Rectification through Vacuum, Phys. Rev. Lett. **104**, 154301 (2010).

[2] H. Reddy, U. Guler, A. V. Kildishev, A. Boltasseva, and V. M. Shalaev, Temperature-dependent optical properties of gold thin films, Opt. Mater. Express **6**, 2776 (2016).

[3] J. A. Briggs, G. V. Naik, Y. Zhao, T. A. Petach, K. Sahasrabuddhe, D. Goldhaber-Gordon, N. A. Melosh, and J. A. Dionne, Temperature-dependent optical properties of titanium nitride, Appl. Phys. Lett. **110**, 101901 (2017).

[4] Z. Wang, D. Kortge, Z. He, J. Song, J. Zhu, C. Lee, H. Wang, and P. Bermel, Selective emitter materials and designs for high-temperature thermophotovoltaic applications, Sol. Energy Mater. Sol. Cells **238**, 111554 (2022).

[5] N. Zhou, X. Xu, A. T. Hammack, B. C. Stipe, K. Gao, W. Scholz, and E. C. Gage, Plasmonic near-field transducer for heat-assisted magnetic recording, Nanophotonics **3**, 141 (2014).

[6] N. P. Padture, M. Gell, and E. H. Jordan, Thermal barrier coatings for gas-turbine engine applications, Science **296**, 280 (2002).

[7] H. G. Liljenvall and A. G. Mathewson, The optical properties of silver in the energy range 3.2-4.3 eV as a function of temperature, J. Phys. C: Solid State Phys. **3**, S341 (1970).

[8] A. M. Brown, R. Sundararaman, P. Narang, W. A. Goddard, and H. A. Atwater, *Ab initio* phonon coupling and optical response of hot electrons in plasmonic metals, Phys. Rev. B **94**, 075120 (2016).

[9] H. Reddy, U. Guler, K. Chaudhuri, A. Dutta, A. V. Kildishev, V. M. Shalaev, and A. Boltasseva, Temperature-dependent optical properties of single crystalline and polycrystalline silver thin films, ACS Photonics **4**, 1083 (2017).

[10] C. F. Klingshirn, *Semiconductor Optics*, Graduate Texts in Physics (Springer, Berlin/Heidelberg, 2012).

[11] G. Cassabois, G. Fugallo, C. Elias, P. Valvin, A. Rousseau, B. Gil, A. Summerfield, C. J. Mellor, T. S. Cheng, L. Eaves, C. T. Foxon, P. H. Beton, M. Lazzeri, A. Segura, and S. V. Novikov, Exciton and Phonon Radiative Linewidths in Monolayer Boron Nitride, Phys. Rev. X **12**, 011057 (2022).

[12] L. Viña, S. Logothetidis, and M. Cardona, Temperature dependence of the dielectric function of germanium, Phys. Rev. B **30**, 1979 (1984).

[13] Z. A. Ibrahim, A. I. Shkrebtii, M. J. G. Lee, K. Vynck, T. Teatro, W. Richter, T. Trepk, and T. Zettler, Temperature dependence of the optical response: Application to bulk GaAs using first-principles molecular dynamics simulations, Phys. Rev. B **77**, 125218 (2008).

[14] A. Marini, *Ab Initio* Finite-Temperature Excitons, Phys. Rev. Lett. **101**, 106405 (2008).

[15] F. Giustino, S. G. Louie, and M. L. Cohen, Electron-Phonon Renormalization of the Direct Band Gap of Diamond, Phys. Rev. Lett. **105**, 265501 (2010).

[16] S. Poncé, G. Antonius, Y. Gillet, P. Boulanger, J. Laflamme Janssen, A. Marini, M. Côté, and X. Gonze, Temperature dependence of electronic eigenenergies in the adiabatic harmonic approximation, Phys. Rev. B **90**, 214304 (2014).

[17] A. Franceschetti, First-principles calculations of the temperature dependence of the band gap of Si nanocrystals, Phys. Rev. B **76**, 161301(R) (2007).

[18] H. Kamisaka, S. V. Kilina, K. Yamashita, and O. V. Prezhdo, *Ab initio* study of temperature and pressure dependence of energy and phonon-induced dephasing of electronic excitations in CdSe and PbSe quantum dots, J. Phys. Chem. C **112**, 7800 (2008).

[19] M. Gajdoš, K. Hummer, G. Kresse, J. Furthmüller, and F. Bechstedt, Linear optical properties in the projector-augmented wave methodology, Phys. Rev. B **73**, 045112 (2006).

[20] Z. M. Zhang, *Nano/Microscale Heat Transfer*, Mechanical Engineering Series (Springer, Berlin/Heidelberg, 2020).

[21] Z. Han, X. Yang, S. E. Sullivan, T. Feng, L. Shi, W. Li, and X. Ruan, Raman Linewidth Contributions from Four-Phonon and Electron-Phonon Interactions in Graphene, Phys. Rev. Lett. **128**, 045901 (2022).

[22] S. Cho, J. Yoon, J.-H. Kim, X. Zhang, A. Manthiram, and H. Wang, Microstructural and electrical properties of $Ce_{0.9}Gd_{0.1}O_{1.95}$ thin-film electrolyte in solid-oxide fuel cells, J. Mater. Res. **26**, 854 (2011).

[23] X. L. Phuah, H. Wang, Z. Qi, S. Misra, M. Kalaswad, and H. Wang, Field assisted heating of Gd doped ceria thin film, J. Am. Ceram. Soc. **103**, 2309 (2020).

[24] A. S. Barker, Transverse and longitudinal optic mode study in MgF_2 and ZnF_2, Phys. Rev. **136**, A1290 (1964).

[25] F. Gervais and B. Piriou, Anharmonicity in several-polar-mode crystals: adjusting phonon self-energy of LO and TO modes in

Al_2O_3 and TiO_2 to fit infrared reflectivity, J. Phys. C: Solid State Phys. **7**, 2374 (1974).

[26] G. Kresse and J. Hafner, *Ab initio* molecular dynamics for liquid metals, Phys. Rev. B **47**, 558 (1993).

[27] A. Togo and I. Tanaka, First principles phonon calculations in materials science, Scr. Mater. **108**, 1 (2015).

[28] W. Li, J. Carrete, N. A. Katcho, and N. Mingo, ShengBTE: A solver of the Boltzmann transport equation for phonons, Comput. Phys. Commun. **185**, 1747 (2014).

[29] Z. Han, X. Yang, W. Li, T. Feng, and X. Ruan, Four-Phonon: An extension module to ShengBTE for computing four-phonon scattering rates and thermal conductivity, Comput. Phys. Commun. **270**, 108179 (2022).

[30] See Supplemental Material at http://link.aps.org/supplemental/10.1103/PhysRevB.107.L201202 for computational details, sample preparations, and optical measurements.

[31] V. I. Anisimov, J. Zaanen, and O. K. Andersen, Band theory and Mott insulators: Hubbard U instead of stoner I, Phys. Rev. B **44**, 943 (1991).

[32] C. Loschen, J. Carrasco, K. M. Neyman, and F. Illas, First-principles LDA+U and GGA+U study of cerium oxides: Dependence on the effective U parameter, Phys. Rev. B **75**, 035115 (2007).

[33] J. Wang, A. Han, S. Jaenicke, and G.-K. Chuah, Advances in Sorbents and Photocatalytic Materials for Water Remediation, in *New and Future Developments in Catalysis*, edited by S. L. Suib (Elsevier Chapters, Amsterdam, 2013).

[34] D. M. D. M. Prabaharan, K. Sadaiyandi, M. Mahendran, and S. Sagadevan, Structural, optical, morphological and dielectric properties of cerium oxide nanoparticles, Mater. Res. **19**, 478 (2016).

[35] M. S. Hybertsen and S. G. Louie, Electron correlation in semiconductors and insulators: Band gaps and quasiparticle energies, Phys. Rev. B **34**, 5390 (1986).

[36] M. Rohlfing and S. G. Louie, Electron-Hole Excitations in Semiconductors and Insulators, Phys. Rev. Lett. **81**, 2312 (1998).

[37] M. Rohlfing and S. G. Louie, Electron-hole excitations and optical spectra from first principles, Phys. Rev. B **62**, 4927 (2000).

[38] J. Deslippe, G. Samsonidze, D. A. Strubbe, M. Jain, M. L. Cohen, and S. G. Louie, BerkeleyGW: A massively parallel computer package for the calculation of the quasiparticle and optical properties of materials and nanostructures, Comput. Phys. Commun. **183**, 1269 (2012).

[39] H. Jiang, R. I. Gomez-Abal, P. Rinke, and M. Scheffler, Localized and Itinerant States in Lanthanide Oxides United by GW @ LDA+U, Phys. Rev. Lett. **102**, 126403 (2009).

[40] H.-Y. Sun, S.-X. Li, and H. Jiang, Pros and cons of the time-dependent hybrid density functional approach for calculating the optical spectra of solids: A case study of CeO_2, Phys. Chem. Chem. Phys. **23**, 16296 (2021).

[41] T. Schäfer, N. Daelman, and N. López, Cerium oxides without U: The role of many-electron correlation, J. Phys. Chem. Lett. **12**, 6277 (2021).

[42] P. B. Allen and M. Cardona, Theory of the temperature dependence of the direct gap of germanium, Phys. Rev. B **23**, 1495 (1981).

[43] J. D. Querales-Flores, J. Cao, S. Fahy, and I. Savić, Temperature effects on the electronic band structure of PbTe from first principles, Phys. Rev. Mater. **3**, 055405 (2019).

[44] S. Poncé, Y. Gillet, J. L. Janssen, A. Marini, M. Verstraete, and X. Gonze, Temperature dependence of the electronic structure of semiconductors and insulators, J. Chem. Phys. **143**, 102813 (2015).

[45] F. Giustino, Electron-phonon interactions from first principles, Rev. Mod. Phys. **89**, 015003 (2017).

[46] H. Kim and M. Kaviany, Effect of thermal disorder on high figure of merit in PbTe, Phys. Rev. B **86**, 045213 (2012).

[47] R. Schwab, R. Steiner, G. Mages, and H.-J. Beie, Properties of CeO_2 and CeO_{2-x} films Part II. High temperature properties, Thin Solid Films **207**, 288 (1992).

[48] Z. M. Gibbs, H. Kim, H. Wang, R. L. White, F. Drymiotis, M. Kaviany, and G. J. Snyder, Temperature dependent band gap in PbX (X = S, Se, Te), Appl. Phys. Lett. **103**, 262109 (2013).

[49] H. Ünlü, A thermodynamic model for determining pressure and temperature effects on the bandgap energies and other properties of some semiconductors, Solid-State Electron. **35**, 1343 (1992).

[50] Y. Cho, A. Yamaguchi, R. Uehara, S. Yasuhara, T. Hoshina, and M. Miyauchi, Temperature dependence on bandgap of semiconductor photocatalysts, J. Chem. Phys. **152**, 231101 (2020).

[51] O. Hellman, P. Steneteg, I. A. Abrikosov, and S. I. Simak, Temperature dependent effective potential method for accurate free energy calculations of solids, Phys. Rev. B **87**, 104111 (2013).

[52] D. S. Kim, O. Hellman, J. Herriman, H. L. Smith, J. Y. Y. Lin, N. Shulumba, J. L. Niedziela, C. W. Li, D. L. Abernathy, and B. Fultz, Nuclear quantum effect with pure anharmonicity and the anomalous thermal expansion of silicon, Proc. Natl. Acad. Sci. **115**, 1992 (2018).

[53] Z. Tong, X. Yang, T. Feng, H. Bao, and X. Ruan, First-principles predictions of temperature-dependent infrared dielectric function of polar materials by including four-phonon scattering and phonon frequency shift, Phys. Rev. B **101**, 125416 (2020).

[54] O. Hellman, I. A. Abrikosov, and S. I. Simak, Lattice dynamics of anharmonic solids from first principles, Phys. Rev. B **84**, 180301(R) (2011).

[55] O. Hellman and I. A. Abrikosov, Temperature-dependent effective third-order interatomic force constants from first principles, Phys. Rev. B **88**, 144301 (2013).

[56] F. Goubin, X. Rocquefelte, M.-H. Whangbo, Y. Montardi, R. Brec, and S. Jobic, Experimental and theoretical characterization of the optical properties of CeO_2, $SrCeO_3$, and Sr_2CeO_4 Containing Ce^{4+} (f^0) Ions, Chem. Mater. **16**, 662 (2004).

[57] M. E. Khalifi, F. Picaud, and M. Bizi, Electronic and optical properties of CeO_2 from first principles calculations, Analytical Methods **8**, 5045 (2016).

[58] P. Patsalas, S. Logothetidis, and C. Metaxa, Optical performance of nanocrystalline transparent ceria films, Appl. Phys. Lett. **81**, 466 (2002).

Supplemental Material for "Temperature-Dependent Full Spectrum Optical Responses of Semiconductors from First Principles"

Zherui Han,[1] Changkyun Lee,[2] Jiawei Song,[3]

Haiyan Wang,[3] Peter Bermel,[2] and Xiulin Ruan[1, *]

[1]*School of Mechanical Engineering and the Birck Nanotechnology Center,*

Purdue University, West Lafayette, Indiana 47907-2088, USA

[2]*School of Electrical and Computer Engineering and the Birck Nanotechnology Center,*

Purdue University, West Lafayette, Indiana 47907-2088, USA

[3]*School of Materials Engineering, Purdue University,*

West Lafayette, Indiana 47907-2088, USA

(Dated: May 4, 2023)

* ruan@purdue.edu

CONTENTS

Sec.1. COMPUTATIONAL DETAILS

In this section, we cover the computational details in our first-principles calculations.

All calculations are done using Density Functional Theory (DFT), Density Functional Perturbation Theory (DFPT) or *ab initio* molecular dynamics (AIMD) as implemented in the VASP package [1]. For structural optimization, we use a Monkhorst k-grid of $12 \times 12 \times 12$ with 520 eV plane wave energy cutoff. Force convergence is within 10^{-6} eV/Å. As described in the main text, we use the local density approximation with Hubbard parameter (LDA+U) approach by setting $U_{\text{eff}} = 10$ eV in this study to correct our band structure [2, 3]. Born effective charges are computed by DFPT and we get $\epsilon_\infty = 5.927$, $Z^*_{Ce,xx} = 5.502$ and $Z^*_{O,xx} = -2.751$ with the aid of Phonopy [4].

Ab initio molecular dynamics are performed on a supercell structure consisting of 192 atoms constructed by $4 \times 4 \times 4$ CeO$_2$ primitive cells. For this size of supercell, only Γ point is computed to accelerate the calculation. After reaching thermal equilibrium under NPT ensemble (zero external pressure) with Langevin thermostat, we use 1000 more steps to get averaged lattice structure at each temperature. An illustration of our temperature control in NPT ensemble is shown in Fig. S1. Then, on relaxed structure we perform NVT ensemble simulations and after reaching equilibrium we use 2000 more steps to construct effective force constants [5] at a time step of 2 fs. Harmonic force constants (HFCs) consider

2

a cutoff radius of 6.31 Å, the third-order force constants have 6 Å and the fourth-order force constants have 4 Å as cutoff.

Optical properties of $4 \times 4 \times 4$ CeO$_2$ supercell are computed in a DPFT manner. We use Γ-centered k-grid of $2 \times 2 \times 2$ and 2560 KS orbitals. This large number of empty bands for transitions is tested for convergence.
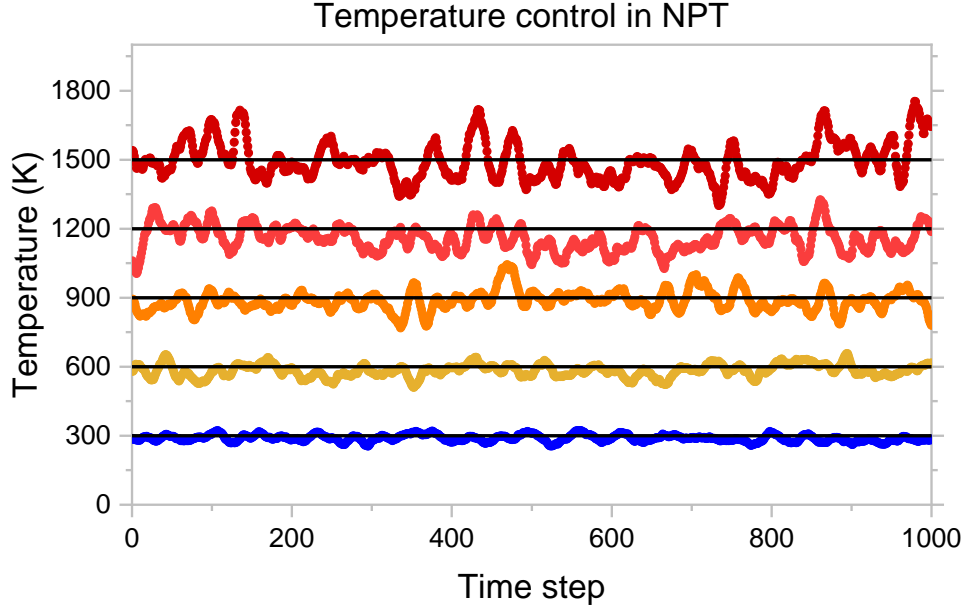

FIG. S1. Temperature fluctuations of NPT ensemble. We report the productive run after reaching equilibrium and we use these steps to calculate the averaged lattice structure.

For phonon-phonon interactions in CeO$_2$, the Brillouin Zone (BZ) is discretized by $15 \times 15 \times 15$ q-mesh to evaluate three-phonon scattering rates using ShengBTE package [6] and $10 \times 10 \times 10$ q-mesh four-phonon scattering rates using FourPhonon tool [7]. In such process, we develop an in-house code to convert TDEP formats to formats that are compatible with our program including the treatment on long-range interactions and boundary conditions. Related tools will be made public when we update FourPhonon tool to next version.

Sec.2. SIMULATED DIELECTRIC FUNCTION AT ROOM TEMPERATURE AND ITS COMPARISON TO EXPERIMENT

Figure. S2 shows our simulated dielectric function at 300 K compared to an electron energy-loss spectroscopy measurement [8] that goes to high photon energy. The change due

3

to temperature is not as apparent as the case at 900 K presented in the main text. The p-f band gap is best reflected by the full temperature effect calculation (solid blue lines). We note that the p-d gap is off by around 1 eV and could be attributed to our large U term in DFT calculations [3].
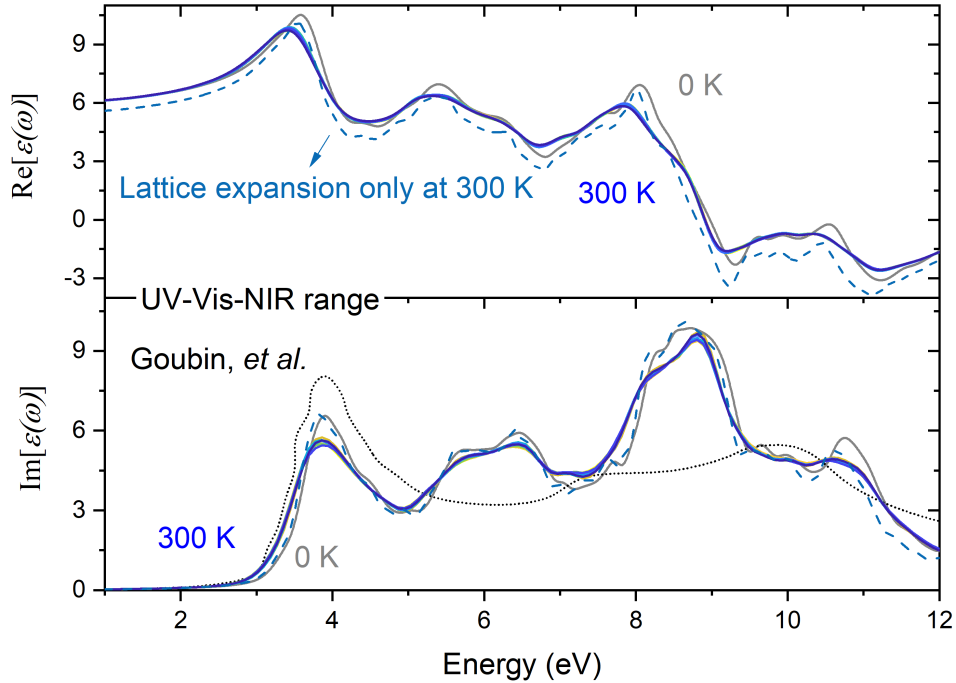

FIG. S2. Room temperature dielectric function. The dotted black line is an experiment work from Ref. [8]. Other legends are consistent with Fig. 2 in the main text.

Sec.3. MEASUREMENTS ON SAMPLE B AND COMPARISONS TO SIMULATIONS

To show the variations of measured optical properties on different sample conditions, we perform the same ellipsometer measurement on another deposited CeO_2 thin film labelled as sample B. The results presented in the main text are based on sample A. The major difference of two samples are that sample A has a thickness of 900 nm while sample B is of 110 nm. The temperature-dependent results measured on sample B are shown in Fig. S3.

It is interesting to find that the measured data well reproduce the peak evolution with temperature (see wavelength below 0.5 μm). High temperature reduces the first refractive peak and in the longer wavelength region this trend progressively shifts to be higher refractive
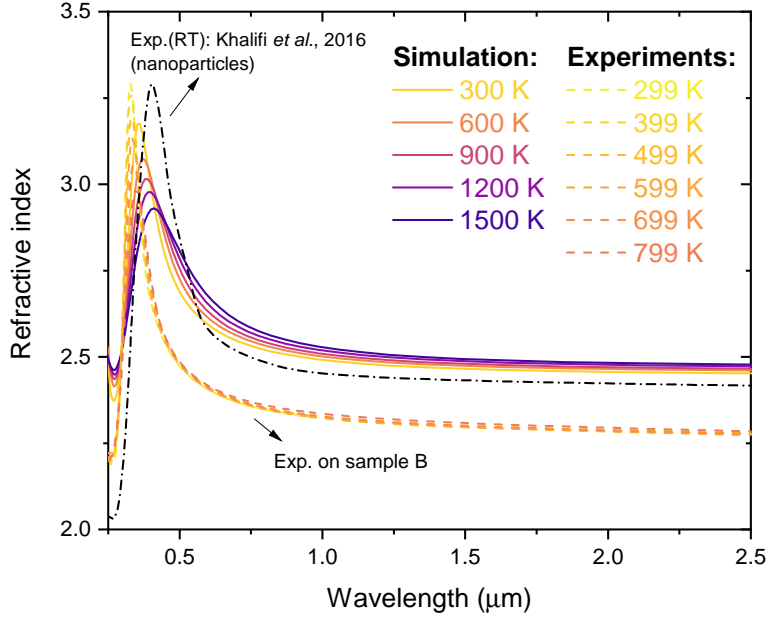
FIG. S3. Temperature-dependent refractive index measured on sample B. Legends are consistent with Fig. 3 in the main text.

index at higher temperature.

In the measurement on sample B, the qualitative agreement is better but the values at IR range are off by about 0.2. This could be due to the surface conditions in thinner sample B that induce some absorption lowering the refractive index. To summarize, our parallel experiments on two different samples show that optical properties are sensitive to sample conditions with various defects, impurities and surface effects. The simulation is based on perfect pristine crystals while the deposited samples are poly-crystalline thin films with different thicknesses: a thicker sample may possess more defects while a thinner sample may be affected by surface impurities. Taking these into account, it is reasonable to argue that our simulation is a good reflection of common features of temperature-dependent optical properties regardless of sample qualities.

Sec.4. ELLIPSOMETER MEASUREMENT SETUP

The ellipsometer measurement setup for two samples are similar with a few differences in temperature control.

We performed the temperature dependent measurement on sample A using variable an-

gular spectroscopic (VASE) integrated with heating cell (INSTEC, HCP621G). The cell is connected to the water cooler (INSTEC, mk2000) and digital heating controller to adjust targeting temperature manually. The heating stage has a gas-tight chamber and and gas ports allow to control and release gas environment. To achieve a stable and accurate environment, the sample was measured after 15 minutes when the heater reached every targeting temperature. The ramp rate to increase the temperature was 5 °C per minute.

For the ellipsometry measurement of sample B, we performed the temperature dependent measurement using the VASE integrated with a special heating stage (Linkam, TSEL 1000). The heating stage has a gas-tight chamber and and gas ports allow to control and release gas environment. The measurement was performed with nitrogen gas under 200 psi. The heating stage was connected to a digital standalone heating controller (Linkam, T96) to heat heater surface. Another cooling method, water circulation pump (Linkam, WCP) was used. The pump is connected to the heating controller instrument bus to actively cool if desired, particularly at high operating temperature. Inside of the heating cell, the pre-embedded retainers and clips were used to tighten and hold the sample in place and improve thermal contact between heater and the sample. The surface of heater surface couldn't interrupt ellipsometry measurement because it was designed to not reflect to the detector. The measurement was performed from 25 °C to 500 °C in steps of 100 °C. The measurement could be only performed at 60° due to the restriction of the heating cell design. To achieve a stable and accurate environment, the sample was measured after 15 minutes when the heater reached every targeting temperature. The ramp rate to increase the temperature was 5 °C per minute.

Sec.5.   SAMPLE PREPARATION

The CeO_2 thin film (targeted thickness of 900 nm for sample A, 110 nm for sample B) was deposited on a STO (001) substrate by using pulsed laser deposition (PLD) with a KrF excimer laser (Lambda Physik, $\lambda = 248$ nm). The substrate temperature was kept at 600 °C and a 20 mTorr oxygen pressure was used during deposition. After deposition, the temperature was naturally cooled down to room temperature at 20 mTorr oxygen partial pressure. The crystallinity and growth orientation was first characterized by X-ray diffraction (XRD). As shown in Fig. S4, the CeO_2 film grows highly textured along (00l) direction on the STO
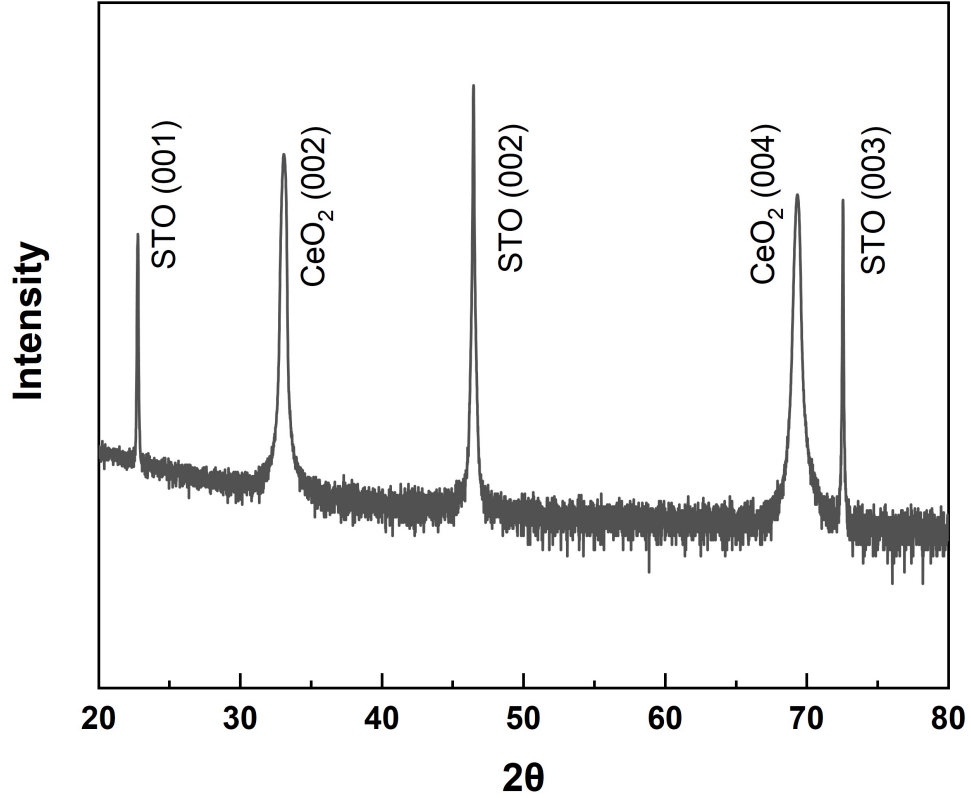
6

FIG. S4. XRD of the CeO_2 film (sample A) grown on STO (001) substrate.

substrate. The sharp peaks suggest good crystallinity of CeO_2 film.

[1] G. Kresse and J. Hafner, Ab initio molecular dynamics for liquid metals, Phys. Rev. B **47**, 558 (1993).

[2] V. I. Anisimov, J. Zaanen, and O. K. Andersen, Band theory and mott insulators: Hubbard u instead of stoner i, Phys. Rev. B **44**, 943 (1991).

[3] C. Loschen, J. Carrasco, K. M. Neyman, and F. Illas, First-principles LDA+U and GGA+U study of cerium oxides: Dependence on the effective U parameter, Phys. Rev. B **75**, 035115 (2007).

[4] A. Togo and I. Tanaka, First principles phonon calculations in materials science, Scr. Mater. **108**, 1 (2015).

[5] O. Hellman and I. A. Abrikosov, Temperature-dependent effective third-order interatomic force constants from first principles, Phys. Rev. B **88**, 144301 (2013).

[6] W. Li, J. Carrete, N. A. Katcho, and N. Mingo, ShengBTE: A solver of the Boltzmann transport equation for phonons, Comput. Phys. Commun. **185**, 1747 (2014).

[7] Z. Han, X. Yang, W. Li, T. Feng, and X. Ruan, FourPhonon: An extension module to Sheng-BTE for computing four-phonon scattering rates and thermal conductivity, Comput. Phys. Commun. **270**, 108179 (2022).

[8] F. Goubin, X. Rocquefelte, M.-H. Whangbo, Y. Montardi, R. Brec, and S. Jobic, Experimental and Theoretical Characterization of the Optical Properties of CeO2, SrCeO3, and Sr2CeO4 Containing Ce4+ (f0) Ions, Chemistry of Materials **16**, 662 (2004).